Journal of Molecular Catalysis A: Chemical 424 (2016) 342–350

Contents lists available at ScienceDirect

Journal of Molecular Catalysis A: Chemical

journal homepage: www.elsevier.com/locate/molcata

Hydrogen production by steam reforming of ethanol over Ni-Sr-Al_2O_3-ZrO_2 aerogel catalyst

Ji Hwan Song, Seung Ju Han, Jaekyeong Yoo, Seungwon Park, Do Heui Kim, In Kyu Song*

School of Chemical and Biological Engineering, Institute of Chemical Processes, Seoul National University, Shinlim-dong, Kwanak-ku, Seoul 151-744, South Korea

ARTICLE INFO

Article history:
Received 16 August 2016
Received in revised form
12 September 2016
Accepted 12 September 2016
Available online 13 September 2016

Keywords:
Hydrogen production
Steam reforming of ethanol
Ni-Sr-Al_2O_3-ZrO_2 aerogel catalyst
Supercritical drying
Nickel surface area

ABSTRACT

Ni-Sr-Al_2O_3-ZrO_2 aerogel (NSAZ-Ae) catalyst was prepared by an one-step epoxide-driven sol-gel method and a subsequent supercritical CO_2 drying method. For comparison, Ni-Sr-Al_2O_3-ZrO_2 xerogel (NSAZ-Xe) catalyst was also prepared by a sol-gel method and a subsequent conventional evaporative drying method. NSAZ-Ae catalyst retained higher surface area and larger pore volume than NSAZ-Xe catalyst. NSAZ-Ae catalyst also showed strong interaction between active metal and support, which led to small nickel particles after the reduction. H_2-TPD (temperature-programmed desorption) results revealed that NSAZ-Ae catalyst with smaller nickel particle size had higher nickel dispersion and higher nickel surface area. In addition, NSAZ-Ae catalyst showed higher ethanol adsorption capacity than NSAZ-Xe catalyst. Performance and stability of the catalyst in the ethanol steam reforming reaction was enhanced with the employment of supercritical drying as observed for NSAZ-Ae catalyst. Enhanced physicochemical property and high nickel surface area (high nickel dispersion) of NSAZ-Ae catalyst led to excellent catalytic activity and stability in the hydrogen production by steam reforming of ethanol.

© 2016 Elsevier B.V. All rights reserved.

1. Introduction

Concerns about environmental problems and shortage of conventional fossil fuels have accelerated researches on alternative energy sources [1,2]. Hydrogen energy is one of the promising candidates of alternative energy sources due to its high specific energy density, ampleness, and eco-friendly nature [3,4]. Apart from the advantages listed above, hydrogen can also be utilized in various industrial fields such as internal engines and fuel cells [5]. Extensive researches have been made on various methods to produce hydrogen in massive scale with efficiency [5,6]. Although industrial-scale hydrogen production is mainly based on methane steam reforming process, ethanol is also gaining attention as a reactant candidate of steam reforming for hydrogen production [7,8]. Ethanol is easy to handle and can be produced from fermentation process of biomass materials [8]. Ideal steam reforming of ethanol occurs as presented in Eq. (1), where ethanol and water react with a stoichiometric factor of $H_2O/C_2H_5OH = 3$ to produce 6 molecules of hydrogen per one ethanol molecule [9].

$$C_2H_5OH + 3H_2O \rightarrow 2CO_2 + 6H_2 \qquad (\Delta H^{\circ}_{29\,K} = +174\,kJ/mol) \quad (1)$$

Various metals have been investigated as active components in the ethanol steam reforming. For example, noble metal-based catalysts such as Rh, Pt, and Pd show high hydrogen yield [10,11]. Application of other transition metals such as Ni and Co to steam reforming of ethanol have also been studied [12,13]. As for supporting materials, extensive researches concerning the usage of mixed-metal oxides, hydrotalcites, and perovskites have been made [14–16]. Among these numerous catalytic systems, nickel catalyst supported on alumina is known to be the most feasible and widely studied catalytic system for ethanol steam reforming, because nickel shows high activity for ethanol steam reforming reaction in spite of its low price [17,18]. Reaction pathways of ethanol steam reforming on the supported nickel catalyst leads to the formation of various carbon-containing intermediates due to ethanol dehydrogenation (Eq. (2)), ethanol decomposition (Eq. (3)), and ethanol dehydration (Eq. (4)) [19].

$$C_2H_5OH \rightarrow CH_3CHO + H_2 \qquad (\Delta H^{\circ}_{29\,K} = +68\,kJ/mol) \quad (2)$$

$$C_2H_5OH \rightarrow CH_4 + CO + H_2 \qquad (\Delta H^{\circ}_{29\,K} = +49\,kJ/mol) \quad (3)$$

$$C_2H_5OH \rightarrow C_2H_4 + H_2O \qquad (\Delta H^{\circ}_{29\,K} = +45\,kJ/mol) \quad (4)$$

Ethylene by-product formed by dehydration of ethanol polymerizes to form carbon species which suppresses activity and stability of the catalyst [20]. Ethanol dehydration has a tendency to be catalyzed on the acid sites of alumina [21]. To solve this problem,

---

* Corresponding author.
E-mail address: inksong@snu.ac.kr (I.K. Song).

http://dx.doi.org/10.1016/j.molcata.2016.09.013
1381-1169/© 2016 Elsevier B.V. All rights reserved.

diverse modifications were made to Ni/Al_2O_3 catalyst. For example, alkaline-earth metal elements have been added to neutralize acid sites of alumina, and thus, to suppress ethanol dehydration and to improve catalytic activity and stability [17]. It has been reported that promotion of Ni/Al_2O_3 catalyst with Mg results in diminished acidity and enhanced nickel dispersion [22]. Addition of other alkaline-earth metal species such as Ca and Sr into Ni/Al_2O_3 catalyst also shows a positive effect in a sense that the reduced acidity leads to lower ethylene selectivity and higher hydrogen yield [23,24]. Apart from alkaline-earth metal, another element widely studied for modification of steam reforming catalyst is zirconium, which forms a mixed metal oxide with alumina support. Introduction of Zr species on Ni/Al_2O_3 is reported to induce enhanced H_2O adsorption/dissociation capacity on the catalyst surface [22,25].

Modification of steam reforming catalyst can be attained by altering chemical compositions and/or by improving textural properties of the catalyst. Development of mesoporous structure within the catalytic system can enhance dispersion of active metal and can increase transfer rate of reactant species [26,27]. Several works concerning the employment of various surfactant materials, which act as a template during the formation of mesoporous structure, have been reported previously [28,29]. For instance, an aerogel catalyst prepared by supercritical drying retains excellent textural properties compared to a xerogel catalyst with the same chemical composition, leading to enhanced catalytic activity of aerogel catalyst [30]. In this respect, direct comparison between aerogel and xerogel forms of Ni-Sr-Al_2O_3-ZrO_2 catalysts for ethanol steam reforming prepared by different drying procedures would be worthwhile.

In this work, Ni-Sr-Al_2O_3-ZrO_2 aerogel (NSAZ-Ae) catalyst was prepared by an epoxide-driven sol-gel method and a subsequent supercritical drying in a stream of CO_2. For comparison, Ni-Sr-Al_2O_3-ZrO_2 xerogel (NSAZ-Xe) catalyst with the same chemical composition was also prepared by an epoxide-driven sol-gel method and a subsequent conventional drying method. The effect of drying method on the physicochemical properties and catalytic activities of Ni-Sr-Al_2O_3-ZrO_2 catalysts in the ethanol steam reforming was investigated.

2. Experimental

2.1. Preparation of catalysts

A mesoporous nickel-strontium-alumina-zirconia aerogel catalyst was prepared by a single-step epoxide-driven sol-gel method followed by a supercritical CO_2 drying [31]. 0.74 g of zirconium precursor (zirconium oxynitrate hydrate, Sigma-Aldrich, 99%) and 0.18 g of strontium precursor (strontium nitrate, Sigma-Aldrich, 99%) were dissolved in 30 ml of ethanol (Solution A). 6 g of aluminum precursor (aluminum nitrate nonahydrate, Sigma-Aldrich, 98%) and 0.89 g of nickel precursor (nickel nitrate hexahydrate, Sigma-Aldrich, 97%) were separately dissolved in 30 ml of ethanol (Solution B). 5 ml and 3 ml of hydrochloric acid (hydrochloric acid, Samchun, 36%) were then added into Solution A and Solution B, respectively. Solution A and Solution B were then mixed under vigorous stirring to obtain a transparent solution (Solution C). After Solution C was further stirred for a few minutes, 25 ml of propylene oxide (Samchun, 99%) was introduced into the solution as a gelation agent. The obtained green opaque gel was aged for 2 days. The resultant gel was then transferred to an autoclave and it went through supercritical CO_2 drying at 50 °C and 120 atm for 12 h. The resulting powder was calcined at 550 °C for 5 h to yield a Ni-Sr-Al_2O_3-ZrO_2 aerogel (denoted as NSAZ-Ae) catalyst. For comparison, a nickel-strontium-alumina-zirconia xerogel catalyst was also prepared with the same procedures mentioned above, except that the resultant gel was dried in a convection oven at 80 °C for 5 days instead of in a supercritical CO_2 stream. The obtained powder was calcined at 550 °C for 5 h to yield a Ni-Sr-Al_2O_3-ZrO_2 xerogel (denoted as NSAZ-Xe) catalyst. In both catalysts, nickel and strontium contents with respect to alumina-zirconia were fixed at 15 wt% and 6 wt%, respectively.

2.2. Characterization

Textural properties of calcined and reduced catalysts were analyzed with nitrogen adsorption-desorption experiments using a BELSORP-mini II (BEL Japan) device. Surface impurities were removed by degassing the samples at 150 °C for 4 h with a vacuum pump prior to nitrogen adsorption-desorption measurements. Calculation of surface area was made by applying the BET (Brunauer-Emmett-Teller) method to the isotherm plots. Chemical compositions of the catalysts were determined by ICP-AES (inductively coupled plasma atomic emission spectroscopy) analyses with an ICPS-100IV (Shimadzu) device. XRD (X-ray diffraction) analyses were carried out with a D-Max2500-PC (Rigaku) device, while the operating conditions were kept at 100 mA and 50 kV with Cu-Kα radiation ($\lambda = 1.541$ Å). For the TPR (temperature-programmed reduction) measurements, 0.03 g of each calcined sample was charged into a quartz reactor. Furnace temperature was then elevated from room temperature to 1000 °C at a rate of 10 °C/min under a flow of hydrogen (2 ml/min) diluted with nitrogen (20 ml/min). TPR profiles were collected using a TCD (thermal conductivity detector) attached to a gas chromatograph (ACME 6000, Younglin). TEM (transmission electron microscopy) images of reduced and used samples were obtained with a JEM-2000EXII device (Jeol). Nickel surface areas of reduced catalysts were calculated from H_2-TPD (temperature-programmed desorption) profiles by assuming that adsorption stoichiometry of H/Ni is 1 and cross-sectional area of single nickel atom is 6.49×10^{-20} m^2. H_2-TPD analyses were conducted with a BELCAT-B instrument (BEL Japan), where 0.02 g of each catalyst was reduced under 5% hydrogen/argon (50 ml/min) at 700 °C for 2 h. Hydrogen adsorption was done by flowing 5% hydrogen/argon flow (50 ml/min) at 50 °C for 30 min, followed by purging the reactor under an argon flow (50 ml/min) at 100 °C for 1 h to remove physisorbed hydrogen molecules. Furnace temperature was increased from 50 °C to 1000 °C at a rate of 5 °C/min under an argon flow (30 ml/min), and the amount of desorbed hydrogen was detected with a TCD. In order to conduct EtOH-TPD experiments, 0.02 g of each catalyst was reduced under a flow of hydrogen (3 ml/min) diluted with helium (30 ml/min) at 700 °C for 2 h. After cooling down the reactor to room temperature, 10 ml of vaporized ethanol was pulsed into the reactor for several times along with 5 ml/min of helium flow to saturate the catalyst surface with ethanol. Physisorbed ethanol was removed by evacuating the sample at 100 °C for 1 h under a flow of helium (15 ml/min). Furnace temperature was elevated from room temperature to 700 °C at a rate of 10 °C/min under a helium flow (10 ml/min). Desorbed species were monitored using a GC–MSD (6890N GC-5975MSD, Agilent) device. Different m/z values were assigned to various desorbed species; 16, 28, 29, 31, and 44 for CH_4, CO, CH_3CHO, C_2H_5OH, and CO_2, respectively. The amount of carbon deposition on the used catalysts was determined by CHNS elemental analyses with a CHNS 932 device (Leco).

2.3. Steam reforming of ethanol

Catalytic activity of NSAZ-Ae and NSAZ-Xe catalysts in the ethanol steam reforming was evaluated in a fixed-bed reactor at 450 °C for 15 h under a continuous flow and atmospheric pressure. Prior to the reaction, 0.05 g of each catalyst sample was reduced at 700 °C for 2 h under a mixed flow of hydrogen (3 ml/min) and nitrogen (30 ml/min). Nitrogen (30 ml/min) was used as a carrier gas during the reforming reaction. A liquid mixture of ethanol and deionized water was continuously introduced into the reactor using a syringe pump (US/KDS-101, KDScientific) at a rate of 0.5 ml/h, where the molar ratio of steam to ethanol in the liquid mixture was fixed at 6. Inlet and the outlet lines of the reactor were heated at 220 °C to maintain a vapor phase. Total feed rate with respect to catalyst weight was set as 46,280 ml/(h g_{cat}). Compositions of reaction products were analyzed using an on-line gas chromatograph (ACME 6000, Younglin) equipped with a TCD. Porapak N and Molecular Sieve 5A columns were used for product separation. Ethanol conversion, hydrogen yield, and selectivity for carbon-containing products were calculated by the following equations, where n_i in Eq. (7) represented the stoichiometric factor of the carbon-containing species.

$$Ethanol\ \ conversion(\%) = \frac{F_{EtOH,in} - F_{EtOH,out}}{F_{EtOH,in}} \times 100 \tag{5}$$

$$Hydrogen\ \ yield(\%) = \frac{F_{H_2,out}}{3 \times (F_{EtOH,in} - F_{EtOH,out})} \times 100 \tag{6}$$

$$S_{i,carbon\ \ containing\ \ product}(\%) = \frac{n_i \times F_{i,carbon\ \ containing\ \ product}}{2 \times (F_{EtOH,in} - F_{EtOH,out})} \times 100 \tag{7}$$

3. Results and discussion

3.1. Characterization of calcined catalysts

Calcined NSAZ-Ae and NSAZ-Xe catalysts were characterized by nitrogen adsorption-desorption measurements. As shown in Fig. 1(a), both NSAZ-Ae and NSAZ-Xe catalysts exhibited type IV isotherms, which were found in samples where capillary condensation occurred in pore structures with mesoporous range [31,32]. However, two samples showed different hysteresis loops. NSAZ-Ae showed H1-type hysteresis loop indicating the presence of pore network formed from spherical agglomerates, while NSAZ-Xe exhibited H2-type hysteresis loop resulting from 'ink-bottle' shaped pore structure [32,33]. This disparity in pore structure between two samples was due to different drying methods employed during the preparation process. In case of NSAZ-Xe, conventional drying of ethanol solvent resulted in shrinkage and rearrangement of pore structure due to vapor-liquid interfacial tension which formed mesopores with smaller pore opening than body [34]. On the other hand, NSAZ-Ae experienced less pore shrinkage, because the solvent was exchanged with liquid CO_2 during the supercritical CO_2 drying process. Fig. 1(b) shows the pore size distributions of the samples. The result showed that NSAZ-Ae retained larger pore size than NSAZ-Xe.

Table 1
Physicochemical properties of NSAZ-Ae and NSAZ-Xe catalysts calcined at 550 °C for 5 h.

Catalyst	Ni content (wt%)[a]	Sr content (wt%)[a]	Surface area (m^2/g)[b]	Pore volume (cm^3/g)[c]	Average pore diameter (nm)
NSAZ-Ae	15.0	6.1	385	1.35	13.7
NSAZ-Xe	14.7	6.3	279	0.56	8.0

[a] Determined by ICP-AES analyses.
[b] Calculated by the BET equation at relative pressure (P/P_0) of 0.05-0.30.
[c] Total pore volume at $P/P_0 \sim 0.990$.

Detailed physicochemical properties of calcined catalysts are summarized in Table 1. Although both samples maintained a mesoporous structure after the calcination process, NSAZ-Ae catalyst retained higher surface area, larger pore volume, and larger average pore diameter than NSAZ-Xe catalyst. This result implies that supercritical drying during the catalyst preparation process was helpful to maintain well-structured mesopores, where the collapse of gel structure was suppressed by effective removal of solvent molecules confined within the gel structure [30]. It was also revealed that actual contents of nickel and strontium in the NSAZ-Ae and NSAZ-Xe catalysts were in good agreement with the designed values.

XRD patterns of calcined NSAZ-Ae and NSAZ-Xe catalysts are presented in Fig. 2. No noticeable diffraction peaks related to alumina, zirconia, and strontium species were detected, indicating that these species were in an amorphous state. The presence of broad NiO diffraction peaks were detected in two catalysts, implying that nickel mainly existed as nickel oxide in both catalysts after the calcination. Existence of a weak peak corresponding to $NiAl_2O_4$ was also observed in the NSAZ-Ae catalyst, indicating that a small portion of nickel was incorporated into Al_2O_3 to form an aluminate phase. Diffraction peaks related to nickel showed a broad shape rather than a sharp form, implying that the mesoporous structure developed in two catalysts prevented the crystallization of nickel or alumina phases during the calcination process.

TPR profiles of NSAZ-Ae and NSAZ-Xe catalysts are presented in Fig. 3. Both catalysts showed a reduction band within the range of 600–700 °C. Reduction of NiO (the major nickel species in Fig. 2) into metallic nickel was responsible for this reduction band [35]. Peak temperatures of reduction bands were 641 °C for NSAZ-Ae and 615 °C for NSAZ-Xe, respectively. TPR profile of NSAZ-Ae also showed a shoulder peak at high temperature region, which was attributed to the reduction of $NiAl_2O_4$ [36]. The above result indicates that the metal-support interaction between alumina and nickel species was stronger in the NSAZ-Ae than in the NSAZ-Xe. NSAZ-Ae catalyst with excellent textural properties is anticipated

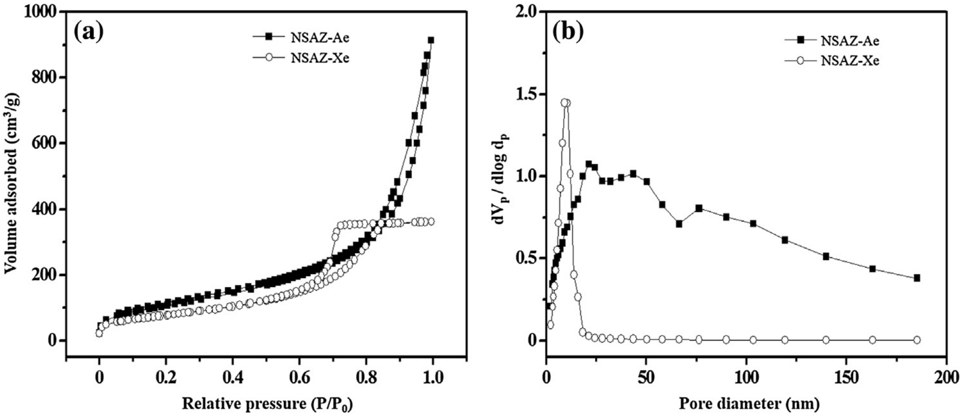

Fig. 1. (a) Nitrogen adsorption-desorption isotherms of NSAZ-Ae and NSAZ-Xe catalysts calcined at 550 °C for 5 h, and (b) BJH pore size distribution plots of the catalysts.

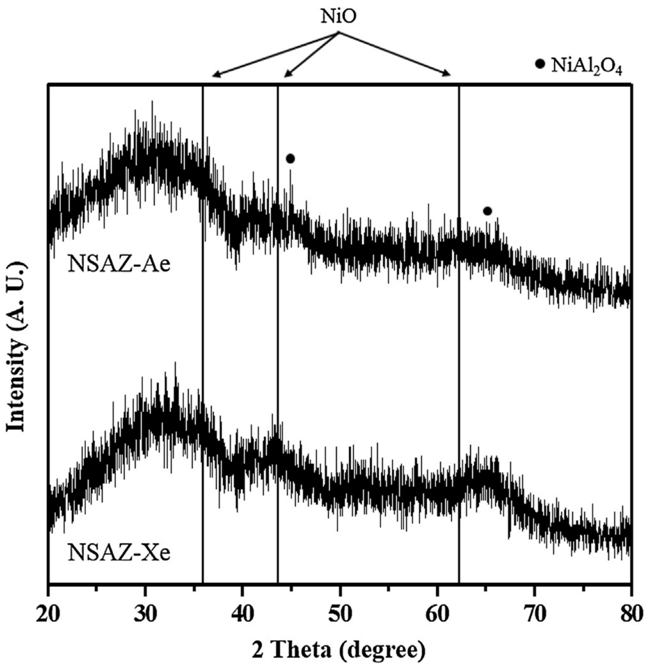

Fig. 2. XRD patterns of NSAZ-Ae and NSAZ-Xe catalysts calcined at 550 °C for 5 h.

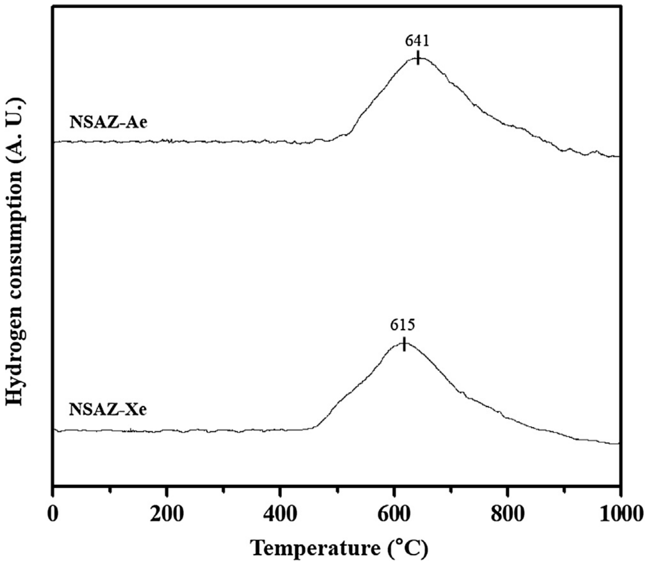

Fig. 3. TPR profiles of NSAZ-Ae and NSAZ-Xe catalysts calcined at 550 °C for 5 h.

to provide the condition for fine dispersion of nickel species, leading to intimate metal-support interaction [37]. Specific reduction bands related to strontium were not detected in both samples.

3.2. Characterization of reduced catalysts

Physicochemical properties of reduced NSAZ-Ae and NSAZ-Xe catalysts were characterized with nitrogen adsorption-desorption measurements as shown in Fig. 4. Both catalysts retained type IV isotherms along with H1-type (NSAZ-Ae) and H2-type (NSAZ-Xe) hysteresis loops (Fig. 4(a)). This indicates that the mesoporous structure was still maintained after the reduction process at high temperature (700 °C). Table 2 summarizes the detailed physicochemical properties of reduced catalysts. Reduced NSAZ-Ae and NSAZ-Xe still retained high surface area (>255 m^2/g), large pore volume (>0.50 cm^3/g), and large average pore diameter (>7.8 nm).

Table 2
Physicochemical properties of NSAZ-Ae and NSAZ-Xe catalysts reduced at 700 °C for 2 h.

Catalyst	Surface area (m^2/g)[a]	Pore volume (cm^3/g)[b]	Average pore diameter (nm)
NSAZ-Ae	315	1.02	13.4
NSAZ-Xe	255	0.50	7.8

[a] Calculated by the BET equation at relative pressure (P/P_0) of 0.05-0.30.
[b] Total pore volume at $P/P_0 \sim 0.990$.

Table 3
Nickel particle size of NSAZ-Ae and NSAZ-Xe catalysts reduced at 700 °C for 2 h.

Catalyst	Particle size (nm)
NSAZ-Ae	6.9
NSAZ-Xe	14.1

[a] Calculated from Ni (2 0 0) diffraction peak in Fig. 5.

However, these physicochemical properties of reduced catalysts showed decreased values when compared to those of calcined catalysts. It is believed that pore blockage due to the release of reduced nickel species from alumina lattice to support surface and sintering due to high temperature might be responsible for diminished physicochemical properties of reduced catalysts [38]. Pore size distributions presented in Fig. 4(b) showed that NSAZ-Ae catalyst still retained larger pore size than NSAZ-Xe catalyst.

Crystalline structures of reduced NSAZ-Ae and NSAZ-Xe catalysts were analyzed with XRD measurements as shown in Fig. 5. Both samples showed sharp peaks indicative of metallic nickel, while diffraction peaks corresponding to other nickel species which were observed before the reduction (Fig. 2) disappeared. This indicates that nickel species in the NSAZ-Ae and NSAZ-Xe were completely reduced into metallic nickel after the reduction. In addition, diffraction peak intensity of metallic nickel of NSAZ-Xe was much stronger than that of NSAZ-Ae. This indicates that NSAZ-Ae retained smaller nickel crystallite particles than NSAZ-Xe. Nickel particle sizes in the reduced catalysts were calculated by applying the Scherrer equation on Ni (2 0 0) peaks of Fig. 5 as presented in Table 3. Higher surface area (Table 1) and stronger metal-support interaction (Fig. 3) of NSAZ-Ae caused better dispersion of nickel species and stronger resistance against sintering, which led to smaller nickel particle size. On the contrary, nickel species in the NSAZ-Xe catalyst were more susceptible to sintering due to weak metal-support interaction, leading to large nickel particle size after the reduction [39]. To confirm the analyses concerning the dispersion and particle size of nickel in the reduced catalysts, TEM images of reduced NSAZ-Ae and NSAZ-Xe were obtained as shown in Fig. 6. It is evident that nickel particles were more finely dispersed in the NSAZ-Ae (Fig. 6(a)) than in the NSAZ-Xe (Fig. 6(b)). Distributions of nickel particle sizes in both samples are shown in Fig. 6. NSAZ-Xe exhibited broader distribution of particle sizes than NSAZ-Ae. No nickel particles larger than 10 nm were observed in the NSAZ-Ae, while a considerable portion of nickel particles in the NSAZ-Xe was larger than 10 nm.

3.3. Nickel surface area of reduced catalysts

Fig. 7 shows the H_2-TPD results of reduced NSAZ-Ae and NSAZ-Xe catalysts. NSAZ-Ae and NSAZ-Xe catalysts showed several desorption peaks reaching over a wide temperature range. To calculate the amount of hydrogen desorbed from metallic nickel sites, H_2-TPD profiles were deconvoluted. Three different domains resulting from deconvolution were attributed to desorbed hydrogen molecules of various identities. First domain with the lowest desorption peak temperature (<300 °C) originates from desorbed hydrogen weakly interacted with nickel sites. Next domain

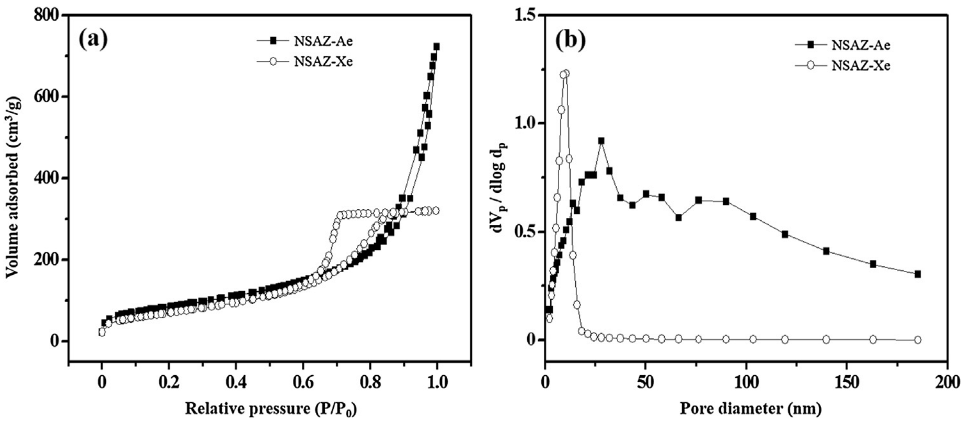

Fig. 4. (a) Nitrogen adsorption-desorption isotherms of NSAZ-Ae and NSAZ-Xe catalysts reduced at 700 °C for 2 h, and (b) BJH pore size distribution plots of the catalysts.

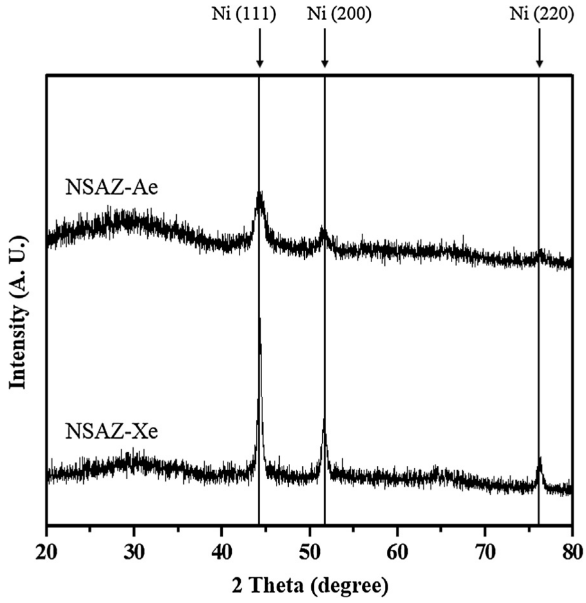

Fig. 5. XRD patterns of NSAZ-Ae and NSAZ-Xe catalysts reduced at 700 °C for 2 h.

with intermediate desorption peak temperature (300–600 °C) is ascribed to desorbed hydrogen which is strongly bonded to metallic nickel. However, the last domain with the highest desorption peak temperature (>600 °C) is due to hydrogen desorbed from the support sublayer as a result of hydrogen spillover [40,41]. Therefore, the last domain at the highest temperature was not considered when calculating the nickel surface area. In other words, the amount of desorbed hydrogen and nickel surface area were calculated from the peak areas of the other two domains attributed to active nickel sites by assuming the adsorption of one hydrogen atom per single active nickel site [41].

The amount of hydrogen desorbed from two domains of the samples and nickel surface area calculated from the amount of desorbed hydrogen are summarized in Table 4. Total amount of hydrogen desorbed from NSAZ-Ae was much larger than that of NSAZ-Xe. Although almost identical amount of nickel species existed in both samples, NSAZ-Ae catalyst exhibited higher nickel surface area. Excellent textural properties of aerogel-based catalyst (NSAZ-Ae) is expected to enable better dispersion of active nickel phase, leading to smaller nickel particle size (Table 3) and higher nickel surface area.

Table 4
H_2-TPD results of NSAZ-Ae and NSAZ-Xe catalysts reduced at 700 °C for 2 h.

Catalyst	Amount of desorbed hydrogen (μmol-H_2/g)[a]			Nickel surface area (m^2/g-Ni)[b]
	Weak site (<300 °C)	Strong site (300–600 °C)	Total	
NSAZ-Ae	19.5	96.6	116.1	60.4
NSAZ-Ae	8.3	42.9	51.2	26.6

[a] Calculated from deconvoluted peak area of H_2-TPD profiles in Fig. 7.
[b] Calculated by assuming H/Ni_{atom} = 1.

3.4. Ethanol adsorption capacity of reduced catalysts

The behavior of reduced NSAZ-Ae and NSAZ-Xe catalysts in the adsorption of ethanol was studied with EtOH-TPD analyses as presented in Fig. 8. Adsorbed ethanol on nickel-based catalyst was desorbed in diverse forms due to various surface reaction pathways [23]. The desorbed species were analyzed with a mass-spectrometer, and thus, desorption profiles of reduced samples were separated into individual signals of C_2H_5OH, CH_4, CH_3CHO, CO, and CO_2 according to m/z value. In both NSAZ-Ae (Fig. 8(a)) and NSAZ-Xe (Fig. 8(b)) catalysts, ethanol ($m/z = 31$) and acetaldehyde ($m/z = 29$) were the first to be desorbed at around 200 °C. When ethanol goes through steam reforming on the surface of nickel catalyst, ethanol is initially adsorbed as an ethoxide form due to dehydrogenation of hydroxyl ($CH_3CH_2O^*$). Then a subsequent dehydrogenation from Cα of the ethoxide species occurs to form acetaldehyde species (CH_3CHO^*) [42]. Desorption profiles of ethanol and acetaldehyde arise as ethanol adsorbed on the catalyst surface is desorbed in its original state or is dehydrogenated to be desorbed as acetaldehyde. Adsorbed acetaldehyde species then goes through C—C bond cleavage to yield adsorbed methyl group, carbon oxides, and hydrogen ($CH_3CHO^* \rightarrow CH_3^* + CO^* + H^*$) [43]. This is related to the fact that other carbon-containing species such as CH_4, CO and CO_2 are then desorbed at higher temperature. In particular, carbon dioxide exhibits desorption peak with the broadest temperature range in both samples, reaching almost up to 550 °C. Sequential dehydrogenation of methyl groups adsorbed on catalyst surface results in carbon species, and these carbon species react with oxygen to produce carbon oxides that is desorbed at sufficiently high temperature [44]. Similarity of NSAZ-Ae and NSAZ-Xe in the sequence of desorbed intermediates with regard to temperature suggests that adsorbed ethanol behaves in an analogous way on the surface of both catalysts.

To calculate the ethanol adsorption capacity of the catalysts, it was assumed that the sum of various desorbed carbon-containing species was equal to the total quantity of adsorbed ethanol ini-

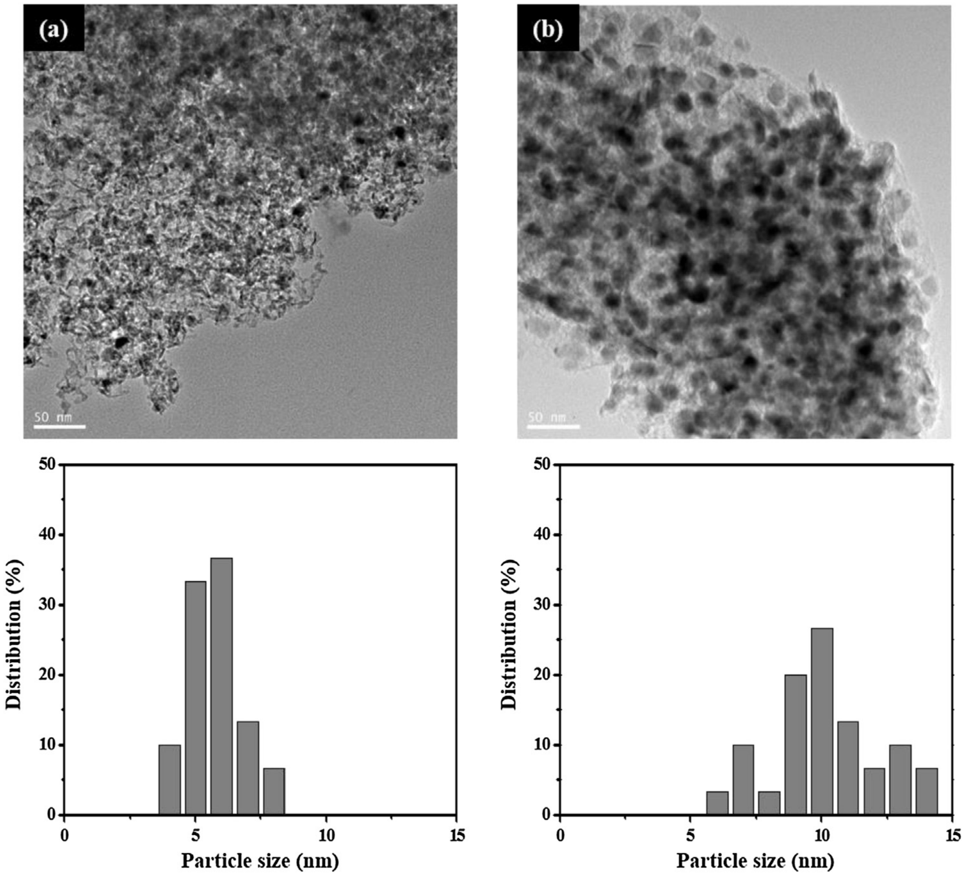

Fig. 6. TEM images and particle size distributions of (a) NSAZ-Ae and (b) NSAZ-Xe catalysts reduced at 700 °C for 2 h.

Table 5
EtOH-TPD results of NSAZ-Ae and NSAZ-Xe catalysts reduced at 700 °C for 2 h.

Catalyst	NSAZ-Ae	NSAZ-Xe
Amount of ethanol adsorbed(mmol-EtOH/g-catalyst)	0.691	0.626

tially existing on the surface of the reduced catalysts. Although each carbon-containing intermediate was assigned according to m/z value, desorbed ethanol ($m/z = 31$) and carbon dioxide ($m/z = 44$) were also known to express weak signals at $m/z = 29$ and $m/z = 28$, respectively. Thus, a portion of acetaldehyde ($m/z = 29$) and carbon monoxide ($m/z = 28$) desorption peaks was regarded as ethanol and carbon dioxide when calculating the amount of desorbed species. Table 5 summarizes the ethanol adsorption capacity of the catalysts. NSAZ-Ae catalyst showed higher capacity for ethanol adsorption than NSAZ-Xe catalyst. Therefore, it is expected that NSAZ-Ae with higher nickel surface area (Table 4) and higher specific surface area (Table 2) provides more active sites where ethanol reactant can adsorb on.

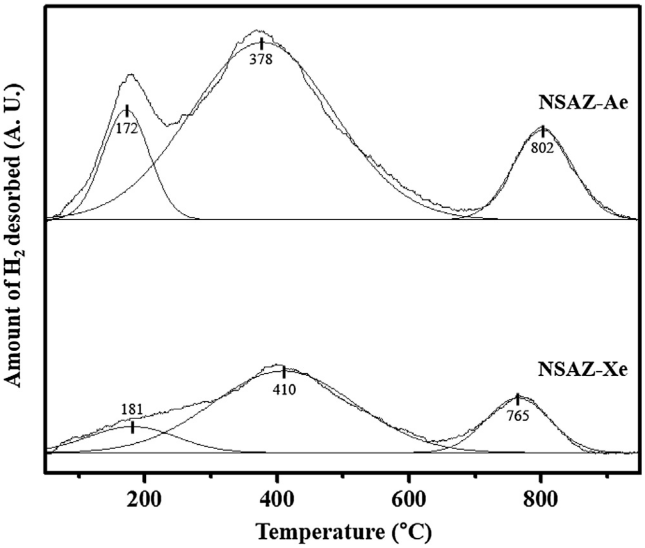

Fig. 7. H_2-TPD profiles of NSAZ-Ae and NSAZ-Xe catalysts reduced at 700 °C for 2 h.

3.5. *Hydrogen production by steam reforming of ethanol*

Catalytic performance of NSAZ-Ae and NSAZ-Xe catalysts in the ethanol steam reforming at 450 °C is shown in Fig. 9. It was revealed that NSAZ-Ae catalyst was more effective in the steam reforming of ethanol, leading to higher hydrogen yield. In addition, NSAZ-Ae catalyst maintained a stable catalytic activity without deactivation for 15 h, while NSAZ-Xe catalyst experienced a slight catalyst deactivation. Thus, introduction of supercritical drying method during the catalyst preparation process had a positive effect in the ethanol steam reforming reaction by increasing activity and stability of NSAZ-Ae catalyst. Excellent textural properties and high nickel dispersion of NSAZ-Ae catalyst were responsible for such improvement. Large pore volume promotes the reactant molecules to be transferred more efficiently during the reforming reaction, while high nickel dispersion provides more accessible active sites where ethanol can preferably adsorb on.

Hydrogen yield, ethanol conversion, and selectivity for by-products after a 15 h-reaction are summarized in Table 6. Ethanol supplied onto the catalysts resulted in complete conversion.

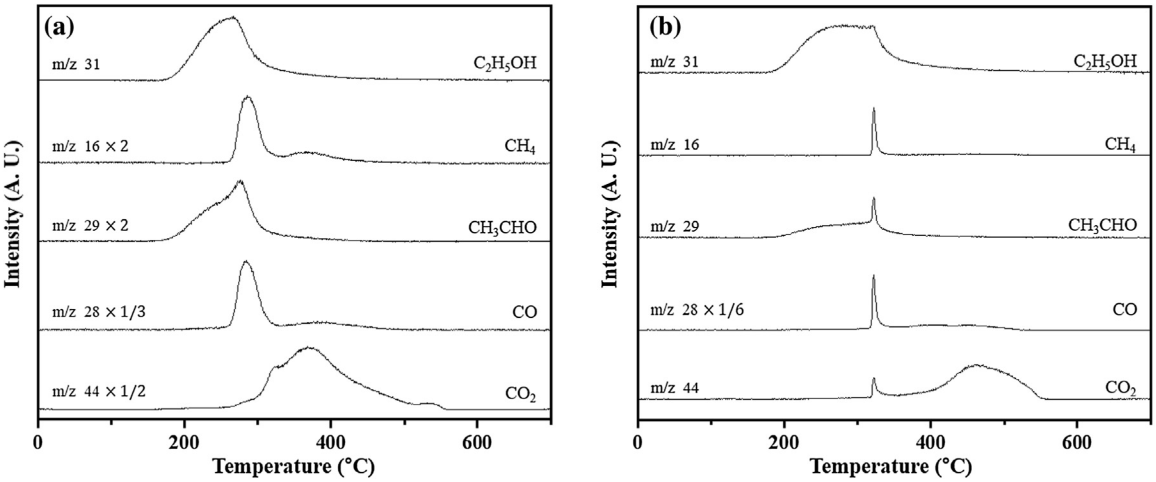

Fig. 8. EtOH-TPD profiles of (a) NSAZ-Ae and (b) NSAZ-Xe catalysts reduced at 700 °C for 2 h.

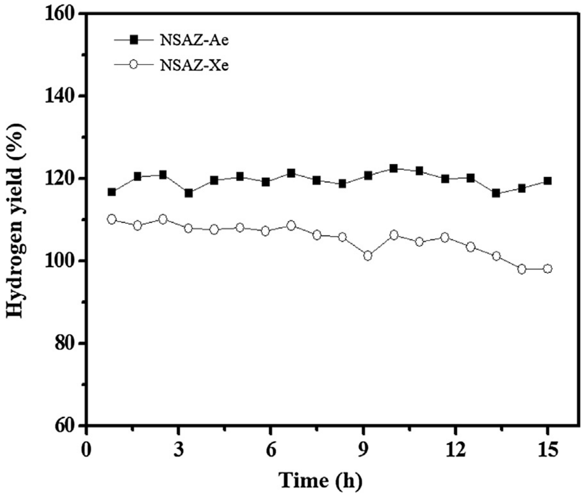

Fig. 9. Hydrogen yield with time on stream in the steam reforming of ethanol over NSAZ-Ae and NSAZ-Xe catalysts at 450 °C. All the catalysts were reduced at 700 °C for 2 h prior to the reaction.

Table 6

Detailed catalytic performance of NSAZ-Ae and NSAZ-Xe catalysts in the steam reforming of ethanol at 450 °C after a 15 h-reaction.

Catalyst	NSAZ-Ae	NSAZ-Xe
Ethanol conversion (%)	100	100
Hydrogen yield (%)	119.4	98.1
Selectivity for CH_4 (%)	24.5	26.3
Selectivity for C_2H_4 (%)	0	0
Selectivity for CO (%)	15.9	24.1
Selectivity for CO_2 (%)	59.6	49.6

Methane, carbon monoxide, and carbon dioxide were formed as intermediate products during the steam reforming reaction. Ethylene formed by ethanol dehydration (Equation (4)) was not detected in the outlet gas over both catalysts, suggesting that ethylene species were reformed and/or acted as a coke precursor on the catalyst surface. There was no great difference in methane selectivity between NSAZ-Ae and NSAZ-Xe. Selectivity for CO over NSAZ-Xe was higher than that over NSAZ-Ae, while CO_2 selectivity was lower. This implies that water-gas shift reaction ($CO + H_2O \rightarrow CO_2 + H_2$) preferentially occurred over NSAZ-Ae catalyst, contributing to high hydrogen yield [45].

Table 7

Amount of carbon deposition on NSAZ-Ae and NSAZ-Xe catalysts after a 15 h-reaction.

Catalyst	NSAZ-Ae	NSAZ-Xe
Amount of carbon deposition (wt%)[a]	56.2	35.7

[a] Determined by CHNS elemental analyses.

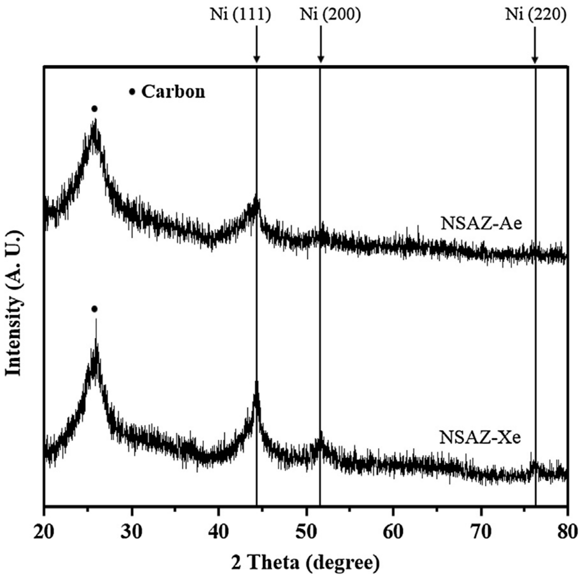

Fig. 10. XRD patterns of NSAZ-Ae and NSAZ-Xe catalysts after a 15 h-reaction.

3.6. Characterization of used catalysts

NSAZ-Ae and NSAZ-Xe catalysts obtained after a 15 h-reaction were characterized with CHNS, XRD, and TEM analyses. The amount of carbon deposition on the used catalysts is summarized in Table 7. NSAZ-Ae catalyst, which exhibited higher hydrogen yield and more stable performance, showed a higher degree of carbon deposition. It is believed that NSAZ-Ae with higher area of exposed catalyst surface also retains more surface acid sites on Al_2O_3 [21], providing the conditions favorable for carbon deposition.

XRD patterns of used NSAZ-Ae and NSAZ-Xe samples are shown in Fig. 10. A strong peak corresponding to carbon was detected in both catalysts due to severe carbon deposition during the ethanol steam reforming reaction. Peak intensity of metallic nickel was still

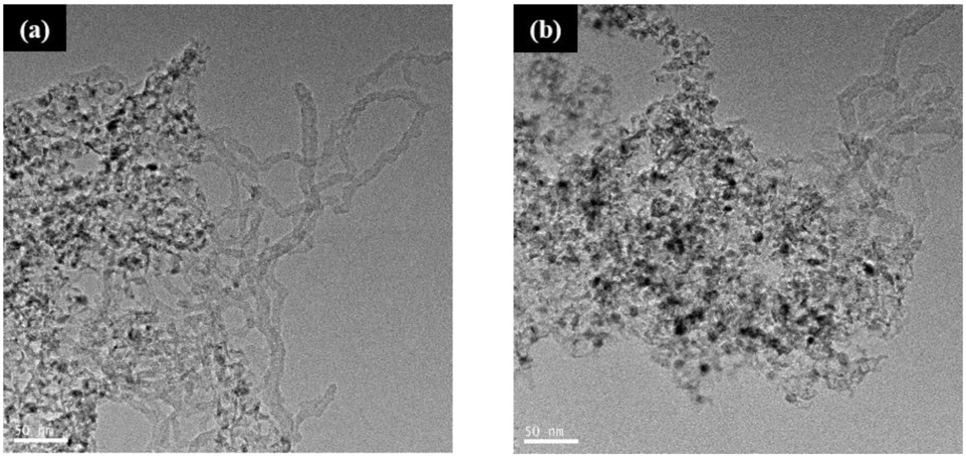

Fig. 11. TEM images of (a) NSAZ-Ae and (b) NSAZ-Xe catalysts after a 15 h-reaction.

stronger in the NSAZ-Xe than in the NSAZ-Ae. However, peak intensity of metallic nickel was attenuated in both catalysts after the reaction when compared to that in Fig. 5. This decrement of peak intensity was due to dilution effect caused by considerable quantity of carbon deposited on NSAZ-Ae and NSAZ-Xe catalysts [46]. TEM images of used NSAZ-Ae (Fig. 11(a)) and NSAZ-Xe (Fig. 11(b)) indicate the formation of filamentous carbon species on both samples after a 15 h-reaction. It is known that filamentous carbon does not pose a severe threat to catalytic activity by encapsulating the active sites in conditions of high H_2/CO or steam/hydrocarbon ratio [47]. Thus, it is expected that carbon deposition on the used NSAZ-Ae and NSAZ-Xe catalysts was not related to encapsulation of nickel, and both catalysts did not suffer from severe deactivation despite the considerable amount of deposited carbon.

4. Conclusions

Ni-Sr-Al_2O_3-ZrO_2 catalysts were prepared by an epoxide-driven sol-gel method. Aerogel-based catalyst (NSAZ-Ae) was obtained via supercritical CO_2 drying of the composite gel. Xerogel-based catalyst (NSAZ-Xe) was obtained via conventional drying. Although both NSAZ-Ae and NSAZ-Xe catalysts maintained well-structured mesopores, NSAZ-Ae retained excellent textural properties compared to NSAZ-Xe. NSAZ-Ae showed stronger interaction between metal and support, maintaining smaller nickel particles after the reduction process. From H_2-TPD analyses, it was revealed that NSAZ-Ae showed higher nickel surface area due to better dispersion state of nickel. Higher nickel surface area was also related to higher ethanol adsorption capacity of NSAZ-Ae catalyst. Catalytic activity and stability of NSAZ-Ae was found to be higher than those of NSAZ-Xe, due to larger amount of active nickel sites and greater affinity toward ethanol of NSAZ-Ae catalyst. It was concluded that aerogel-based Ni-Sr-Al_2O_3-ZrO_2 catalyst (NSAZ-Ae) prepared by a supercritical drying method served as an efficient ethanol steam reforming catalyst.

Acknowledgement

This work was supported by the Global Frontier R&D Program on Center for Multiscale Energy System funded by the National Research Foundation under the Ministry of Science, ICT & Future Planning, Korea (20110031575).

References

[1] M.S. Dresselhaus, I.L. Thomas, Nature 414 (2001) 332–337.
[2] A. Haryanto, S. Fernando, N. Murali, S. Adhikari, Energy Fuels 19 (2005) 2098–2106.
[3] K. Mazloomi, C. Gomes, Renew. Sustain. Energy Rev. 16 (2012) 3024–3033.
[4] M. Momirlan, T.N. Veziroglu, Int. J. Hydrogen Energy 30 (2005) 795–802.
[5] W. Lubitz, W. Tumas, Chem. Rev. 107 (2007) 3900–3903.
[6] K. Takeishi, H. Suzuki, Appl. Catal. A: Gen. 260 (2004) 111–117.
[7] K. Vasudeva, N. Mitra, P. Umasankar, S.C. Dhingra, Int. J. Hydrogen Energy 21 (1996) 13–18.
[8] M. Benito, J.L. Sanz, R. Isabel, R. Padilla, R. Arjona, L. Daza, J. Power Sources 151 (2005) 11–17.
[9] C. Montero, A. Ochoa, P. Castaño, J. Bilbao, A.G. Gayubo, J. Catal. 331 (2015) 181–192.
[10] A.C. Basagiannis, P. Panagiotopoulou, X.E. Verykios, Top. Catal. 51 (2008) 2–12.
[11] S. Cavallaro, V. Chiodo, S. Freni, N. Mondello, F. Frusteri, Appl. Catal. A: Gen. 249 (2003) 119–128.
[12] C.C. Hung, S.L. Chen, Y.K. Liao, C.H. Chen, J.H. Wang, Int. J. Hydrogen Energy 37 (2012) 4955–4966.
[13] R. Padilla, M. Benito, L. Rodrigues, G. Muñoz, L. Daza, Int. J. Hydrogen Energy 35 (2010) 8921–8928.
[14] S.M. de Lima, A.M. Silva, I.O. da Cruz, G. Jacobs, B.H. Davis, L.V. Mattos, F.B. Noronha, Catal. Today 138 (2008) 162–168.
[15] S.M. de Lima, A.M. da Silva, L.O.O. da Costa, J.M. Assaf, L.V. Mattos, R. Sarkari, A. Venugopal, F.B. Noronha, Appl. Catal. B: Environ. 121 (2012) 1–9.
[16] L. Barattini, G. Ramis, C. Resini, G. Busca, M. Sisani, U. Constantino, J. Chem. Eng. 153 (2009) 43–49.
[17] R. Trane-Restrup, S. Dahl, A.D. Jensen, Int. J. Hydrogen Energy 38 (2013) 15105–15118.
[18] J.R. Rostrup-Nielsen, J. Sehested, J.K. Nørskov, Adv. Catal. 47 (2002) 65–139.
[19] M.H. Youn, J.G. Seo, H. Lee, Y. Bang, J.S. Chung, I.K. Song, Appl. Catal. B: Environ. 98 (2010) 57–64.
[20] D.L. Trimm, Catal. Today 49 (1999) 3–10.
[21] H.S. Bengaard, J.K. Nørskov, J. Sehested, B.S. Clausen, L.P. Nielsen, A.M. Molenbroek, J.R. Rostrup-Nielsen, J. Catal. 209 (2002) 365–384.
[22] M.C. Sánchez-Sánchez, R.M. Navarro, J.L.G. Fierro, Catal. Today 129 (2007) 336–345.
[23] C.K.S. Choong, L. Huang, Z. Zhong, J. Lin, L. Hong, L. Chen, Appl. Catal. A: Gen. 407 (2011) 155–162.
[24] J.H. Song, S.J. Han, J. Yoo, S. Park, D.H. Kim, I.K. Song, J. Mol. Catal. A: Chem. 418–419 (2016) 68–77.
[25] S. Therdthianwong, A. Therdthianwong, C. Siangchin, S. Yongprapat, Int. J. Hydrogen Energy 33 (2008) 991–999.
[26] Z.-X. Li, F.-B. Shi, L.-L. Li, T. Zhang, C.-H. Yan, Phys. Chem. Chem. Phys. 13 (2011) 2488–2491.
[27] J.G. Seo, M.H. Youn, J.C. Jung, I.K. Song, Int. J. Hydrogen Energy 35 (2010) 6738–6746.
[28] W. Li, Q. Yue, Y. Deng, D. Zhao, Adv. Mater. 25 (2013) 5129–5152.
[29] S.J. Han, Y. Bang, J. Yoo, S. Park, K.H. Kang, J.H. Choi, J.H. Song, I.K. Song, Int. J. Hydrogen Energy 39 (2014) 10445–10453.
[30] Y. Bang, S.J. Han, J. Yoo, S. Park, J.H. Choi, Y.J. Lee, J.H. Song, I.K. Song, Int. J. Hydrogen Energy 39 (2014) 4909–4916.
[31] K.S.W. Sing, D.H. Everett, R.A.W. Haul, L. Moscou, R.A. Pierotti, J. Rouquerol, T. Siemieniewska, Pure Appl. Chem. 57 (1985) 603–619.
[32] G. Leofanti, M. Padovan, G. Tozzola, B. Venturelli, Catal. Today 41 (1998) 207–219.
[33] T.F. Baumann, A.E. Gash, S.C. Chinn, A.M. Sawvel, R.S. Maxwell, J.H. Satcher, Chem. Mater. 17 (2005) 395–401.
[34] C.L. Glaves, C.J. Brinker, D.M. Smith, P.J. Davis, Chem. Mater. 1 (1989) 34–40.
[35] J.M. Rynkowski, T. Paryjczak, M. Lenik, Appl. Catal. A: Gen. 106 (1993) 73–82.
[36] J. Zieliński, J. Catal. 76 (1982) 157–163.

[37] B. Mile, D. Stirling, M.A. Zammitt, A. Lovell, M. Webb, J. Catal. 114 (1988) 217–229.
[38] J. Yoo, Y. Bang, S.J. Han, T.H. Kang, J. Lee, I.K. Song, J. Mol. Catal. A: Chem. 380 (2013) 28–33.
[39] C.K.S. Choong, Z. Zhong, L. Huang, Z. Wang, T.P. Ang, A. Borgna, J. Lin, L. Hong, L. Chen, Appl. Catal. A: Gen. 407 (2011) 145–154.
[40] Y. Cesteros, P. Salagre, F. Medina, J.E. Sueiras, Appl. Catal. B: Environ. 25 (2000) 213–227.
[41] S. Velu, S.K. Gangwal, Solid State Ionics 177 (2006) 803–811.
[42] D. Zanchet, J.B.O. Santos, S. Damyanova, J.M.R. Gallo, J.M.C. Bueno, ACS Catal. 5 (2015) 3841–3863.
[43] A.N. Fatsikostas, X.E. Verykios, J. Catal. 225 (2004) 439–452.
[44] A.L. Alberton, M.M.V.M. Souza, M. Schmal, Catal. Today 123 (2007) 257–264.
[45] S.J. Han, Y. Bang, J. Yoo, K.H. Kang, J.H. Song, J.G. Seo, I.K. Song, Int. J. Hydrogen Energy 38 (2013) 15119–15127.
[46] A. Carrero, J.A. Calles, A.J. Vizcaíno, J. Chem. Eng. 163 (2010) 395–402.
[47] C.H. Bartholomew, Appl. Catal. A: Gen. 212 (2001) 17–60.